

Controlled Preferential Oxidation of Grain Boundaries in Monolayer WS₂ for Direct Optical Imaging

Youmin Rong¹, Kuang He¹, Mercè Pacios¹, Alex W. Robertson¹, Harish Bhaskaran¹, Jamie H. Warner^{1}*

¹Department of Materials, University of Oxford, Parks Road, Oxford, OX1 3PH, United Kingdom

*Jamie.warner@materials.ox.ac.uk;

RECEIVED DATE

Abstract

Synthetic 2D crystal films growth by chemical vapour deposition are typically polycrystalline and determining grain size within domains and continuous films is crucial for determining their structure. Here we show that grain boundaries in the 2D transition metal dichalcogenide WS₂, grown by CVD can be preferentially oxidized by controlled heating in air. Under our developed conditions, the bulk WS₂ remains relatively unaffected, whilst preferential degradation at the grain boundaries causes an increase in their physical size due to oxidation. This increase in size enables their clear and rapid identification using a standard optical microscope. We demonstrate that similar treatments in Ar environment do not show this effect, confirming that oxidation is the main role in the structural change. Statistical analysis of grain boundary angles shows dominant mirror formation. Electrical biasing across the GB is shown to also lead changes at the GB and their observation under an optical microscope. Our approach enables high-throughput screening of as-synthesized WS₂ domains and continuous films to determine their crystallinity and should enable improvements in future CVD growth of these materials.

KEYWORDS: WS₂, Grain Boundaries, 2D crystals, TMDs, 2D materials.

Development of chemical vapour deposition (CVD) techniques has enabled the growth of large-scale high-quality two-dimensional (2D) materials such as single-atom-thick graphene.¹⁻⁴ However, grain boundaries (GBs) in the as-synthesized 2D films are easily formed due to merger of randomly oriented crystalline domains during the growth of the polycrystalline films.^{5,6} The GBs play an important role in influencing electron transport properties.^{4,7-10} Therefore there is an urgent need for not only realizing lateral GB distributions across a given sized sample, but also being able to detect them on a large-scale and in a time-efficient manner. GBs in graphene have been extensively imaged and studied at the atomic scale using transmission electron microscopy (TEM)^{11,12} or scanning tunnelling microscopy (STM).^{7,13,14} This approach is only limited to studying small regions of the sample and was substantially improved in terms of the through-put and area examined by using optical microscopy for graphene GBs directly on copper. This was achieved by a straightforward moisture-rich oxidation to the sample.¹⁵

Recent advancement in CVD for producing two-dimensional metal dichalcogenide (TMDs) domains and thin films over large areas,¹⁶⁻²⁰ and application of these 2D TMDs in optical studies²¹⁻²⁴ and optoelectronics,²⁵⁻²⁸ have promoted the need for determining their grain boundaries. GBs and grain structures of monolayer MoS₂ have been successfully examined using colour-coded overlay of dark-field-TEM images.⁸ GBs in WS₂ domains on sapphire substrates were made partially visible by scanning electron microscopy (SEM) using mild oxidation under moisture-rich ambient conditions, taking up to 20 days to emerge.²⁹ However this was a random process with no control and took excessively long for GBs to emerge as visible. Several parts of the WS₂ domains also showed deterioration, making the unambiguous assignment of the GBs challenging. Recent work has shown that UV exposure leads to deterioration of the GBs in TMDs, and it is likely that this is the driving cause of GB deterioration when TMDs are left in room lights and in air.³⁰ The GBs of the 2D materials are not easily detectable using optical microscopy because of their nanometre-sized widths.^{16-18,31,32} An

approach to reveal GBs in 2D TMDs directly on as-deposited substrates with rapid through-put time using large area examination methods such as imaging by optical microscopy is still important.

Results and Discussion

Here we demonstrate a reproducible rapid technique for revealing GBs in CVD grown monolayer WS₂ domains and continuous films on SiO₂/Si substrates under a standard optical microscope. This controlled approach relies on simple heating in air to cause preferential structural changes localised on the WS₂ GBs, shown schematically in Figure 1a. High quality CVD growth of TMDs provides isolated domains that can grow from between 20~400 μm . However, detecting the size of the grains within TMD continuous films has been limited due to the absence of suitable techniques that can detect the GBs on the micron to mm scale. We have improved our recently reported CVD approach to enable control either isolated domain or continuous film growth of WS₂ monolayers (see supporting Figure S1). This gives us the ability to probe both types of TMD crystal forms, isolated single crystals or polycrystalline films. Raman spectroscopy and photoluminescence spectroscopy confirmed that both the isolated domains and the continuous films are predominantly monolayer (supporting Figure S2). We explored several heating conditions to reach the conclusion that 20 minutes at 380°C provided both rapid transformation and achieving clear GB appearance. Figures 1b and 1c show that before heat treatment there are no lines of contrast, but after heat treatment strong contrast lines associated with GBs appear in the WS₂. For isolated WS₂ domains there are several shapes grown during the CVD. In Figure 1c we show the results from heating a perfect triangular shaped domain, most likely a single crystal, and then two multi-faceted structures, likely formed from several crystals merging together. Multi-faceted WS₂ domains after heat treatment show strong contrast lines in locations where one would expect GBs to have formed based on the faceted structures. In contrast, the single crystal triangle in Figure 1c does not show any contrast lines after heat treatment, which provides strong indication that the contrast lines are GBs. The heat treatment of the continuous films shows

similar strong contrast lines and we can extrapolate from our findings that these lines are the GBs in these films.

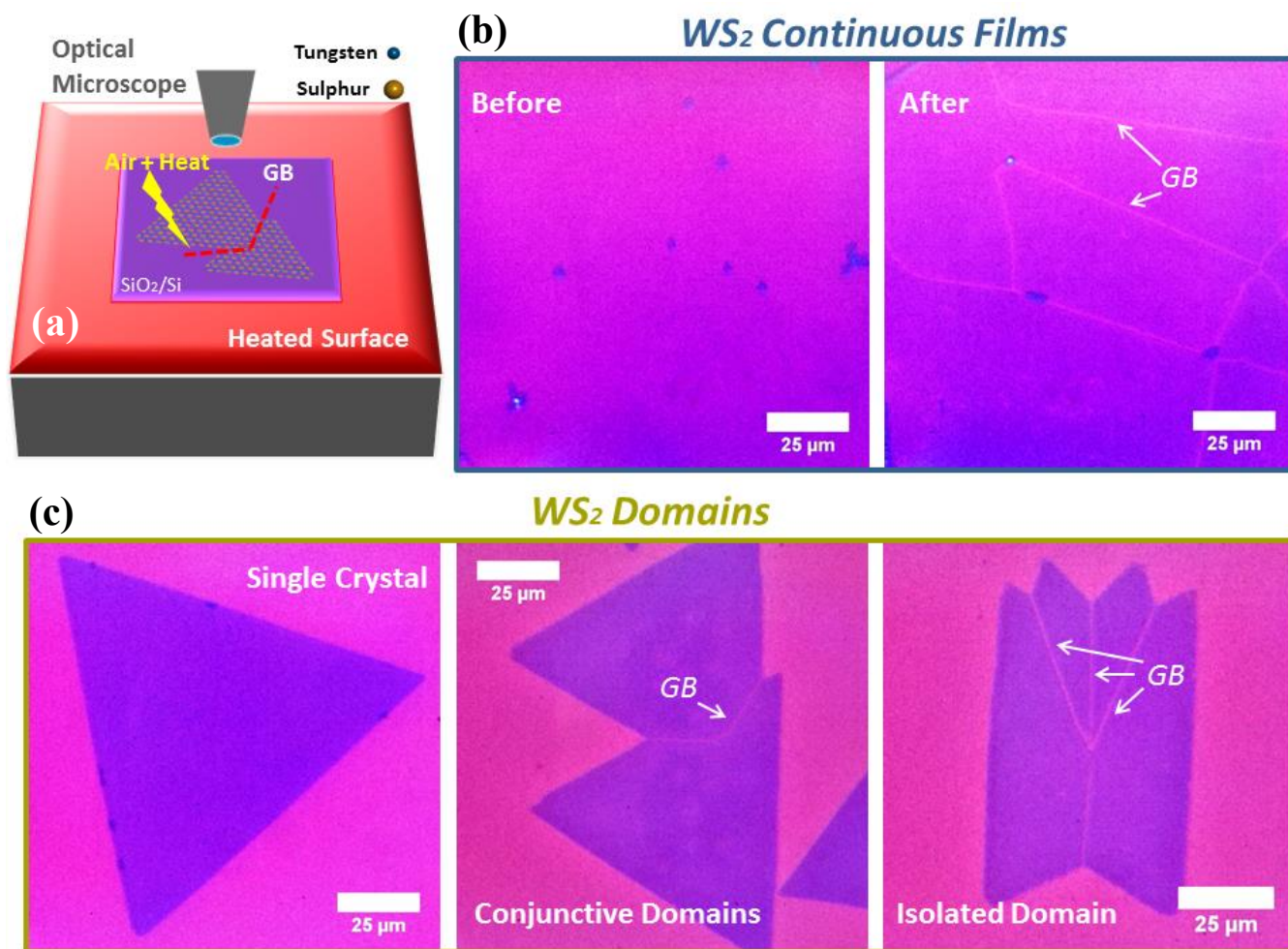


Figure 1. Grain boundaries revealed in monolayer WS₂ continuous films and crystalline domains using the as-developed thermal treatment in air (380°C for 20 min) and observed by an optical microscope. (a) A schematic illustration of the thermal treatment that enabled direct imaging of WS₂ GBs using optical microscope. (b) Optical images of monolayer WS₂ continuous film before and after the thermal treatment in air, resulting in the appearance of WS₂ GBs. (c) Optical images of WS₂ GBs in other monolayer configurations of the as-formed WS₂ crystal which can be generally summarized as single crystal, conjunctive domains and isolated domain.

We used selected area electron diffraction (SAED) within a TEM to map out the crystal structure within two connected monolayer WS₂ domains transferred onto a holey SiN TEM grid, Figure 2. A hole was introduced into the WS₂ using the 80kV electron beam and the atomic resolution image taken by an

aberration-corrected TEM, Figure 2b, shows the hole opens to vacuum, confirming it is monolayer thickness. Examination of the back folded WS₂ edge also only shows a single line of contrast, expected for folded monolayer 2D materials, Figure 2c. Taking SAED patterns from each hole provides accurate tracking of the crystal orientation and reveals a grain boundary running through locations A43, B26 and between C31 and C32 (Figure 2e-n). The as-transferred WS₂ domain has only two crystal orientations across approximately ~324μm (see supporting Figure S3). This confirms our findings in Figure 1. Another example of GB mapping by SAED measurements also confirms the findings, supporting Figure S4.

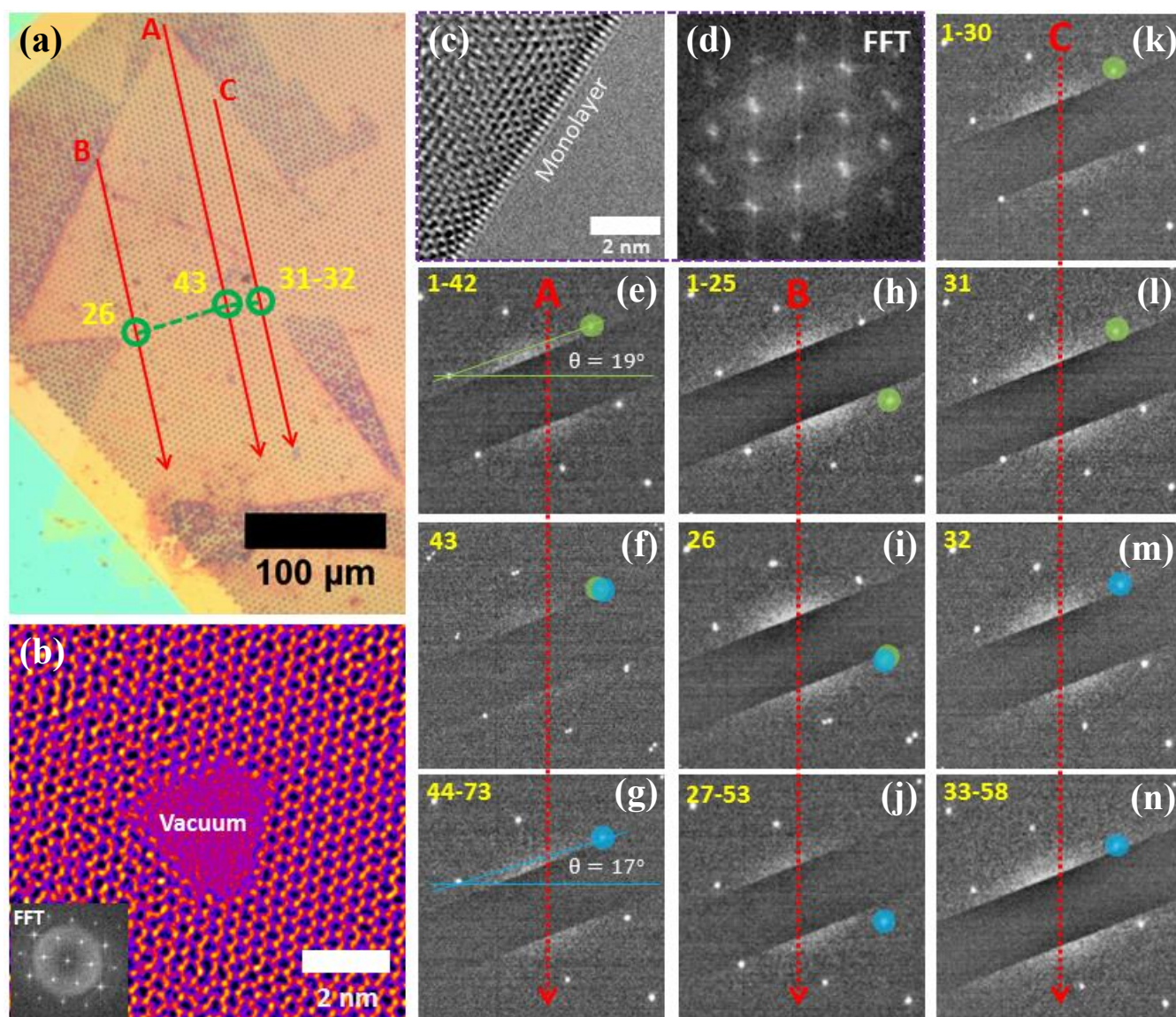


Figure 2. TEM characterizations of monolayer WS₂ domains with regard to the GB locations and crystallinity performed on a holey SiN TEM grid. (a) Optical microscopy image of a WS₂ domain transferred onto the SiN TEM grid with highlighted (red) hole-arrays (A, B and C) for SAED characterisations. Green circles indicate as-determined WS₂ GB positions across the domain with highlighted numbered holes for corresponding SAED diffractions patterns in (f), (i), (l) and (m) respectively. (b) Aberration-corrected (AC)-TEM image of the WS₂ domain showing a hexagonal lattice structure with a hole created by electron beam to show it is a monolayer and the corresponding FFT pattern is introduced in the inset (A colour look-up-table of ‘Fire’ is used to improve visual inspection). (c) A smoothed AC-TEM image taken on the back folded edge of a monolayer WS₂ with (d) showing its corresponding FFT image. (e) - (g) SAED diffraction patterns taken from the hole-array A which span from hole number 1 to 73. (h) - (j) SAED patterns obtained from hole number 1 to 53 of the hole-array B. (k)-(n) Hole number 1 to 58 SAED patterns acquired from the hole-array C. The corresponding WS₂ crystal orientations relative to the horizontal level are presented in (e) and (g) as 19° in green and 17° in blue respectively, which also applies to the colour coding in figure (h) to (n). This SiN TEM grid has a hole-centre to adjacent hole-centre distance of 4.5µm.

We have carried an extensive study of how heating temperature in air over time is affecting the appearance of WS₂ GBs under optical microscopy (as demonstrated in supporting Figure S5). Figure 3a depicts the unveiling of GBs in monolayer WS₂ domains after 90 min exposure to the heating temperature of 250°C in air. If the heating temperature is lower than 250°C, in our study, the GBs in WS₂ domains are not observable with optical microscopy after 90 min. On the other hand, the efficiency of this particular approach can be much improved by having a higher heating temperature as shown in Figure 3b. By treating the WS₂ domains at 380°C in air, the amount time needed for GBs to be visible by optical microscope can be shortened to 20 min. This provided a pathway for more time-efficient GB imaging of monolayer WS₂ domains or films in this context. Further increase to the heating temperature or prolongation to the treating duration can eventually result in damaging the crystal domains instead allowing only GBs to mildly develop (supporting Figure S6) and makes the unambiguous identification of GBs challenging. In addition to the control of heating temperature, the

environment for monolayer WS₂ domains or films to be processed in is also of great importance. Figure 3c demonstrates that using the same heating temperature and the same duration as in Figure 3b but processing instead in an Ar atmosphere led to failure in observing WS₂ GBs optically. This reveals that the thermal treatment for the GB imaging of monolayer WS₂ domains with optical microscopy should be done in an oxidizing atmosphere.

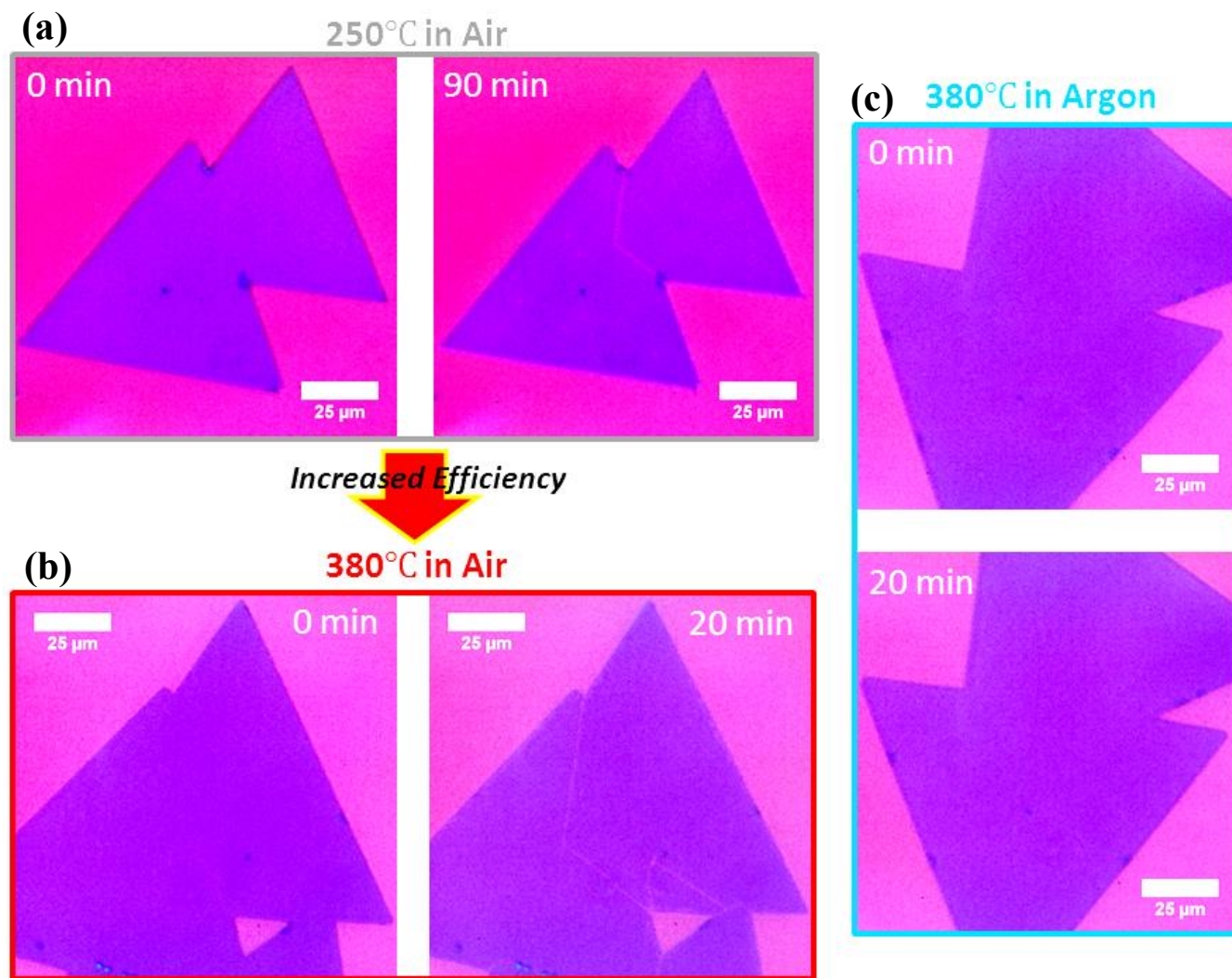


Figure 3. Optical images of WS₂ domains showing the effect of time and heating temperature in air or in inert argon atmosphere on GB visualization. (a) Before and after 90 min in air at a heating temperature of 250°C. (b) Before and after 20 min in air at a heating temperature of 380°C. (c) Before and after 20 min in argon at the heating temperature of 380°C.

Raman spectroscopy and PL spectroscopy was used to probe the GBs after the heat treatment, Figure 4. Figure 4a shows that there is a small decrease in PL peak intensity of the bulk region of the treated WS₂ domains compared to the pristine domains. Moreover, the PL emission of the GBs of the treated WS₂ shows nearly a two-fold decrease in signal relative to that of the central part of the treated domains. Thermal treatment with air may cause adsorption of O₂/H₂O from air or defect creation due to applied thermal energy at WS₂ GBs, which may result in either PL enhancement^{33,34} or quenching.^{8,29} We have found only a small peak shift of 1 nm between the pristine and treated WS₂ domains. We were also able to detect the WS₂ GBs from a PL map of a treated domain, Figure 4b. (i.e. PL mapping was generated by plotting integrated PL peak intensities against XY coordinates where multi-point PL analysis was carried in that specific area of the WS₂ domain.) Raman spectroscopy and 2D Raman mapping can also detect changes of crystallinity either in monolayer WS₂ domains or GBs after heating in air at the designated temperature, Figure 4c-f. The pristine and treated WS₂ domains show similar monolayer characteristic Raman profiles of WS₂ with an in-plane vibrational (E_{2g}^1) mode $\sim 351\text{ cm}^{-1}$ and the out-of-plane vibrational (A_{1g}) mode $\sim 418\text{ cm}^{-1}$, with no peak shifting or quenched intensities observed.³⁵ For the treated WS₂ GBs, the intensity of E_{2g}^1 and A_{1g} peaks reduced by two-fold as compared to the central part of the treated WS₂ domains (and pristine WS₂ domains). Similar to the PL mapping of WS₂ GBs, both E_{2g}^1 and A_{1g} peak intensities from the treated GBs can be used in 2D Raman mapping to see the GBs, Figure 4d and 4e. In addition, the WS₂ GBs after the treatment can also be mapped out using the ratio of E_{2g}^1 to A_{1g} , Figure 4f. Without heating the WS₂ domains, as we have done, PL and Raman 2D mappings cannot clearly reveal the GBs (supporting Figure S7).^{17,29}

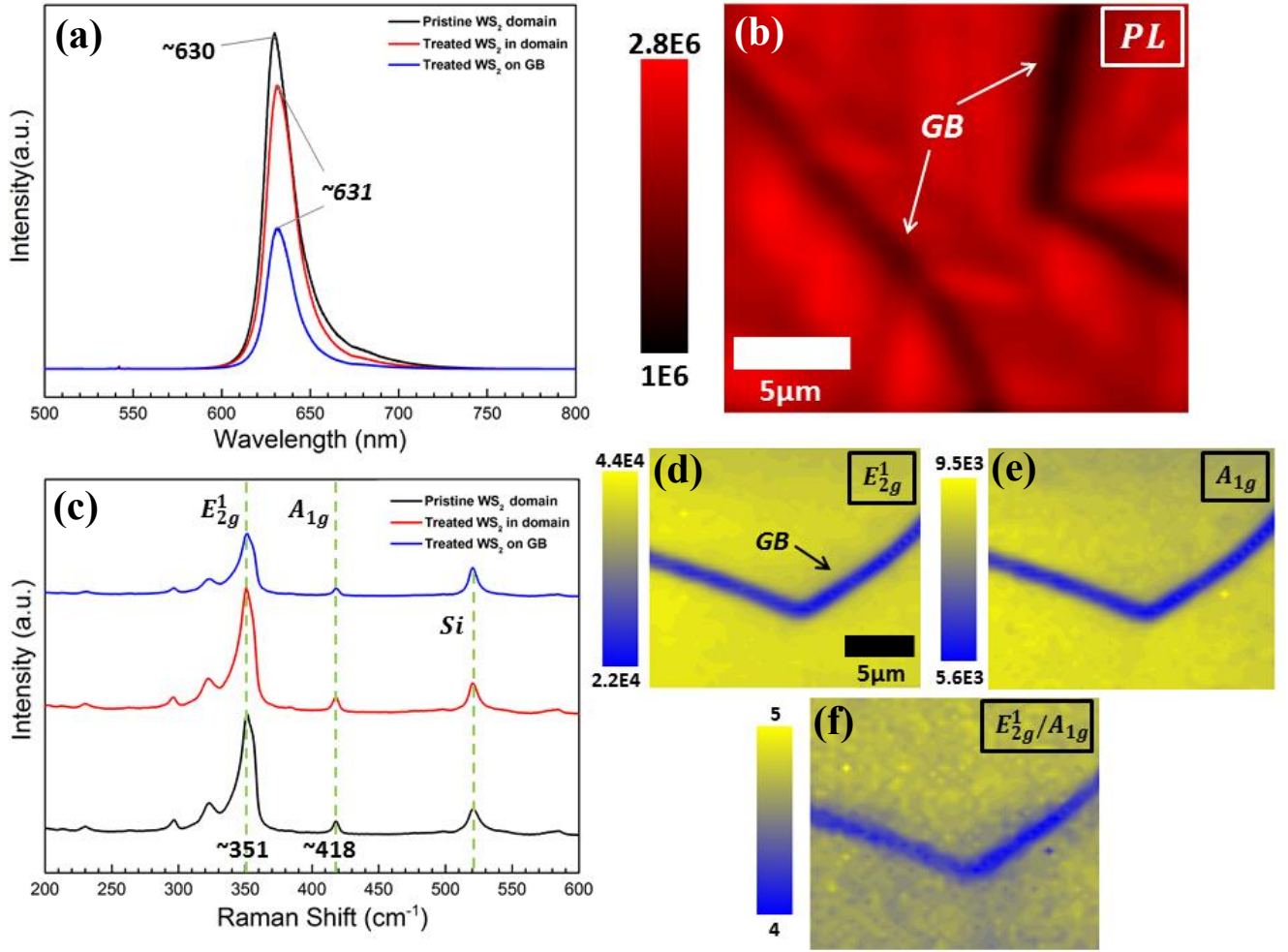


Figure 4. PL and Raman characterizations for as-treated monolayer WS₂ domains at a 532nm excitation laser. (a) PL emission profiles obtained in a pristine monolayer WS₂ domain as opposed to the treated monolayer WS₂ on GB or in domain. (b) PL 2D mapping of the as-developed WS₂ GBs according to the integrated characteristic photon emission intensities from wavelengths 600 to 660 nm. (c) Raman spectra obtained in a pristine monolayer WS₂ domain in comparison with the treated monolayer WS₂ on GB or in domain, with highlighted Si peak and WS₂ characteristic peaks, E_{2g}¹ and A_{1g}. (d) Raman 2D mapping of the WS₂ GBs with regard to the integrated characteristic E_{2g}¹ peak intensities from 330 to 370 cm⁻¹. (e) Raman mapping of the WS₂ GBs executed for the A_{1g} characteristic peak with integrated intensities from 400 to 430 cm⁻¹. (f) Raman mapping of the WS₂ GBs corresponding to the ratio of integrated E_{2g}¹ peak intensities (330-370 cm⁻¹) / integrated A_{1g} peak intensities (400-430 cm⁻¹).

GBs in as-produced high quality CVD monolayer WS_2 domains and polycrystalline films are difficult to detect even under SEM, Figure 5a. However, in certain cases of CVD growth of 2D TMD crystals, some contrast can be detected from the GBs under SEM^{29,36} or optical microscopy^{10,32} due to unwanted multi-layer crystal growth or contamination, as shown in the case of Figure 5b.^{10,36} After our controlled heat treatment in air, the strong contrast (blisters) from the GBs in SEM (Figure 5c) may arise from balling of as-formed WO_x in GB defect area due to reduction of surface energy. Atomic force microscopy (AFM) revealed that the GBs increased in width after heating in air, Figure 5d-i. The actual width of the GB after heating, Figure 5g, is approximately $0.55\mu\text{m}$, Figure 5i, which is large enough to be detected under an optical microscope.¹⁵

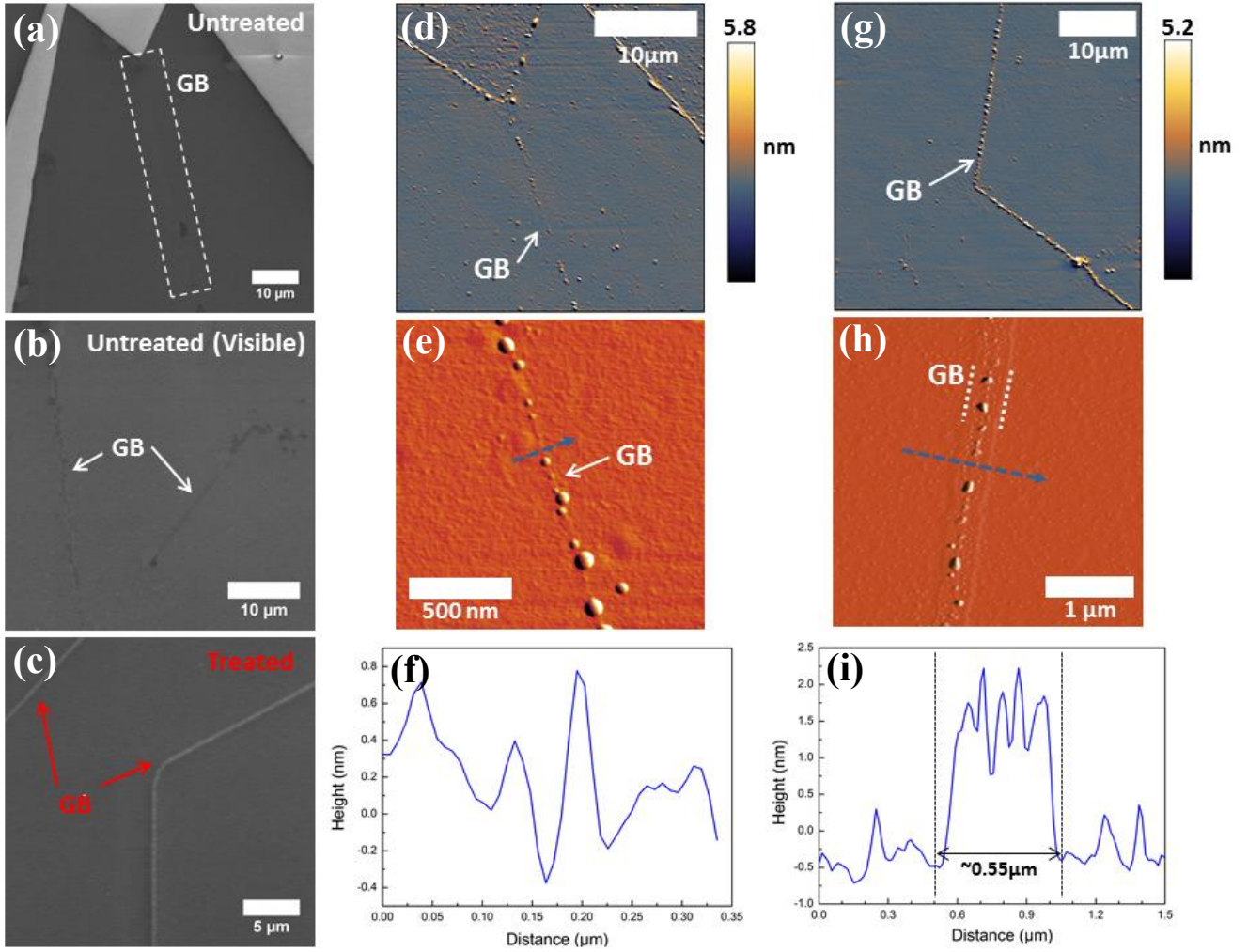


Figure 5. Topological characterisations of the treated WS_2 GBs using SEM and AFM. (a) Untreated WS_2 GBs that are invisible under the SEM observation. (b) Untreated WS_2 GBs that are partially visible with SEM. (c)

Treated WS₂ GBs that show strong contrast with SEM. (d) AFM topological mapping of the untreated WS₂ GB. (e) A closer-up mapping of the untreated WS₂ GB. (f) The corresponding line profile indicated (blue) in (e). (g) AFM topological mapping of the as-treated WS₂ GBs. (h) A finer AFM mapping specifically carried for determination of the topology within the as-treated WS₂ GBs. (i) The as-obtained topological line profile indicated (blue) in (h).

The ability to measure the GBs in a large number of WS₂ domains under an optical microscope enabled a statistical study of their relative orientation with respect to the WS₂ triangle orientation. We found that mirror GBs (i.e GB formed at half angle (θ) of the two neighbouring domain zigzag edge (α)) dominated (Figure 6a). Figure 6b plots the α/θ ratio distribution for 100 GBs measured in oxidized-treated joined domains, fitted with the Lorentz curve (Red). In Figure 6c, typical optical images of GBs are shown, emphasizing that the α/θ ratio is mostly 2. The creation of GB defects occurs when one single crystal merges with another single crystal of different orientation (Figure 6d-e). Whilst the GBs may appear straight at the microscopic level, previous work using STEM has shown that mirror GBs are predominantly consisted of lines of 8- and 4-membered rings at atomic level in MoS₂ (Figure 6e).^{8,37} In addition to van der Zande et al.'s STEM findings of mirror GBs,⁸ our high through-put GB viewing technique has led to not only determining mirror GB as a stellar structure in CVD growth but also understanding that mirror GBs can exist in all domain morphologies.

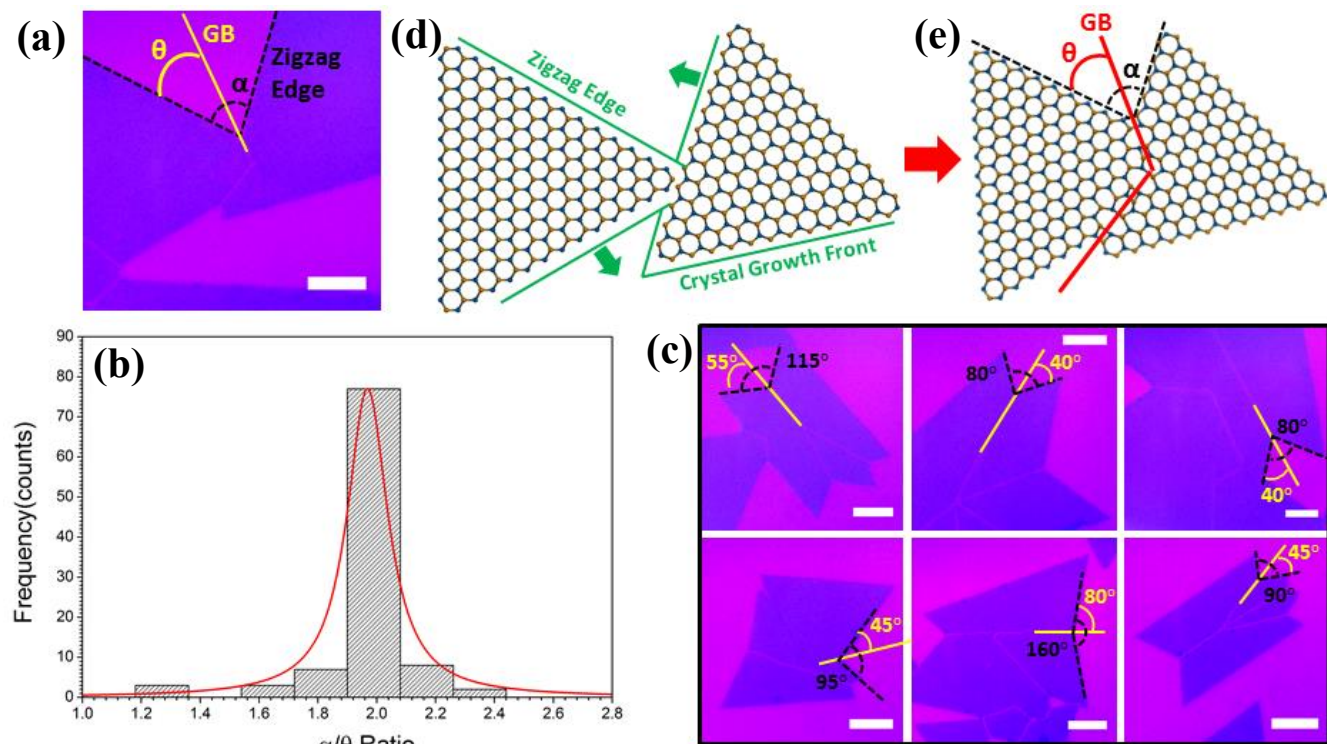


Figure 6. Preferential GB orientations incurred from mismatching of as-grown monolayer WS₂ domains.

(a) A schematic illustration of GB angle (θ = angle between GB and the neighbouring domain edge) bisecting domain angle (α = angle between two neighbouring zigzag edges). Scale bar = 20 μ m (b) Domain angle (α)/GB angle (θ) ratio distribution in 100 monolayer WS₂ domains obtained from our CVD approach. (c) Optical images showing that the majority of GB θ angles bisect the domain α angles in as-synthesized WS₂ joined domains (All scale bars are 20 μ m). (d) Schematic illustration of two pristine WS₂ triangular single crystals with zigzag edges merging together to form a GB. (e) Schematic atomic model showing the formation of GB structure at an orientation that bisects the domain edge angle.

The large size of the CVD-grown WS₂ domains enable electrical contacts using sharp W probes in a probe-station brought directly into the crystals without any lithography needed and thus reduces contamination. Figure 7a and b show the typical IV electrical properties of the as-grown WS₂ domain as well as domains that were oxidised in air. Probes were placed in specified regions likely to be the same crystal to ensure no grain boundary would lie in-between the probes. Both pristine and heat-treated WS₂ domains are conductive at applied source-drain bias of 10V onwards (i.e. a current compliance of 500 nA was used to avoid excess current that heats the sample and causes irreversible deterioration). The W

probes form a Schottky barrier with the WS₂ and result in the non-linear IV curve and large onset bias voltage. The similar IV response of the WS₂ before and after oxidization shows that the material conductivity of WS₂ domain after heat treatment was not greatly affected by the mild oxidation.

Electrical measurements were then taken across a GB for the as-grown WS₂ domains by placing the probe tips either side of a GB. Upon applying the bias, current started to flow, as in the case of the non-GB area, but surprisingly, the GB started to emerge visibly under the optical microscope after a period of current flow, shown in the sequence of images in Figure 7c. The optically invisible GB junction at two domains was found vulnerable to further increase of source-drain bias until two domains became fully separated at the GB site. The corresponding IV measurement shown in Figure 7d monitors how the level of current across the WS₂ GB increases at first (source-drain bias Stage I to IV), but then drops suddenly to zero when source-drain bias reaches ~30V and remains zero for further ramping of source-drain bias (Stage V to VI). This correlates in the optical images of Figure 7c to the increase of WS₂ GB width resulting in formation of two isolated WS₂ domain with no current flowing between. To further study this, W probes were placed either side of a GB made visible by the heat-treatment process in a WS₂ and bias was applied to monitor the IV response. Figure 7e shows that no current flows across the oxidized GB as the bias is increased, but that the width of the GB increases substantially after ramping the bias up to 40V (as in Figure 7c). Another identical example is provided in supporting Figure S8. We repeated these measurements on more than 100 domains and found qualitatively consistent behaviour.

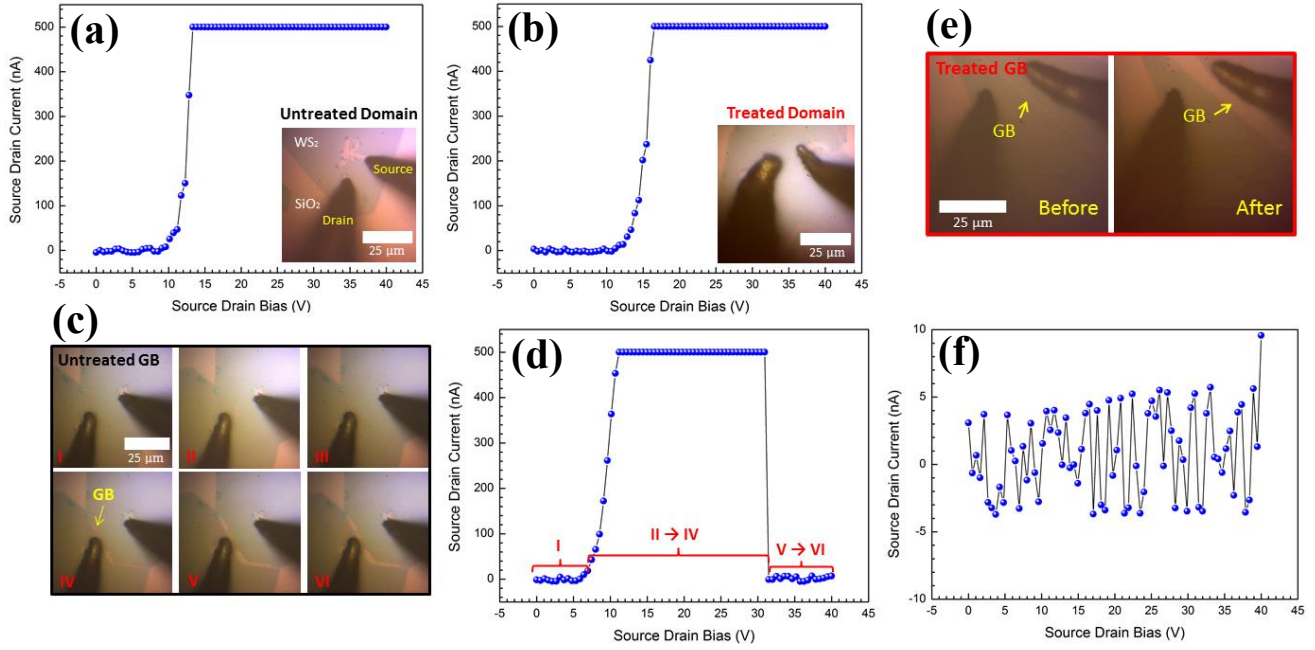


Figure 7. IV source-drain electrical measurements of monolayer WS₂ against its domain (or GB) that is pristine and heat-treated respectively. (a)-(b) The output $I_{sd}V_{sd}$ curves of as-grown WS₂ domain that is unprocessed and processed by the heat treatment in air respectively. (c) Optical images I to VI showing untreated WS₂ GB being revealed under optical microscope at elevated source-drain biases applied against the pristine GB. (d) The corresponding output profile of the untreated WS₂ GB showing in (c). (e) Optical images showing before and after applying source-drain bias against thermally treated WS₂ GB. (f) The corresponding output profile of the WS₂ GB presented in (e). All measurements were conducted at source-drain-bias increase rate of approx. 1.24V/s.

These results show that not only controlled heat treatment of WS₂ domains can lead to the GB becoming visible under the optical microscope through an oxidization process, but also that applying a relatively large bias also causes the GB to become visible. During the biasing across a GB, current flows in the GB area that is likely to represent the location of largest resistance. The higher resistance at the GB might cause increased heating localized to this area and instigate an oxidization process, similar to the heat-treatment process we developed. This is important when considering the operation of WS₂ based field effect transistors in air where similar effects might occur if current levels are high. If we limit current flow across the GB by implementing a severe compliance value (i.e 10nA) then this GB degradation does not occur, indicating that it is related to some form of joule heating at the GB and not

driven by the electric field alone. On the other hand, the increase of GB width in Figure 7e results from heat localization in the W tip area rather than at the GB area. When current does not flow in between a GB, a leaking current through SiO₂ substrate (large resistance) will generate heat to that WS₂ region, resulting in further oxidation of WS₂ domain close to the GB.

Conclusion

The combination of diffraction mapping, optical imaging, Raman and PL mapping, and AFM has revealed that simply heating WS₂ domains in air at the right temperature for a short 20 minute burst causes the GBs to increased and observed using a standard optical microscope. This demonstrates that the grain boundary, which is known to contain defects, has lower oxidation reaction temperature than the bulk crystal. The process works for both domains and polycrystalline films and is high through-put, large area and does not require any fancy equipment of preparation. The ease of this approach should enable its uptake across the community for TMD 2D materials to provide a robust way of determining the degree of polycrystallinity of continuous large area films and can be implemented on the cm scale. Knowing the grain size of TMD films will help correlations between electronic performance and structure, and should lead to the rapid improvement of continuous TMD films by CVD growth, which is critical to their further development in opto-electronics.

Methods

CVD Synthesis of monolayer WS₂

The monolayer WS₂ domains and continuous films were fabricated by adopting the sulphur pre-introduction protocols recently reported by Rong *et al.*¹⁷ However, rather having sulphur and WO₃ precursors placed in a same tube, we optimised the system by separating them using a double-walled-quartz-tube CVD set-up (supporting Figure S1). This has successfully prevented sulphur vapour from reacting with WO₃ powder, which has led to the growth of WS₂ continuous films. Sulphur powder (400

mg of purum grade $\geq 99.5\%$) was placed in the outer tube at 180°C whereas WO_3 powder (200mg of puriss grade 99.9%) was positioned in the inner tube at 1070°C . SiO_2/Si (90 nm) substrates were positioned 10 cm away at the downstream of WO_3 . Argon flow rate of 250 sccm was used for transporting WO_3 and sulphur vapours to the designated substrates. The growth was initiated by ramping sulphur at $\sim 30^{\circ}\text{C}/\text{min}$ and WO_3 at $\sim 40^{\circ}\text{C}/\text{min}$, and giving 3 min reaction time for domain growth or 5 min reaction time for continuous film growth after reaching the target reaction temperature (1070°C). The as-deposited WS_2 samples were fast cooled as soon as the reaction finished.

Transfer of WS_2 domains

The as-produced samples were first spin-coated with a PMMA scaffold (8 wt% in anisole, 495k molecular weight) at 4700 rpm for 60 s and then cured at 150°C for 15 min. The underlying SiO_2/Si substrates were subsequently detached by floating the sample on a 1M KOH (Sigma-Aldrich reagent grade 90%) solution at room temperature. The floating PMMA/ WS_2 films were carefully cleaned by several DI water baths. With regard to the TEM characterization, the PMMA/ WS_2 films were transferred onto holy silicon nitride (SiN) TEM grids (Agar Scientific Y5385) and left to dry overnight in air. PMMA/ WS_2/SiN was subsequently baked at 150°C for 15 min to improve sample adhesion. Lastly, TEM samples were prepared ready after removing PMMA using a 2h acetone solution bath at 45°C .

Treatment of WS_2 for GB optical imaging

In order to unveil GBs in WS_2 domains and continuous films, the as-prepared WS_2 samples were heated in air by placing them at the centre of a Carbolite 1-inch tubular furnace (MTF 12/38A). Samples were removed instantly from the furnace when the treatment was finished and left to cool in air spontaneously. Subsequently, as-treated samples were imaged instantly with the optical microscope at our disposal. In the experiment of Ar-rich atmosphere for WS_2 GB treatment, we prepared the environment by flushing 500 sccm Ar for 1 hr in a 1-inch quartz tube CVD before ramping up the

furnace to 380°C. The thermal treatment to the WS₂ sample was then carried at 380°C for 20 min with only 10 sccm Ar flowing.

Characterization of as-treated WS₂ domains

The optical images of WS₂ GBs in domains and films were taken by an eVue Pro 40X digital imaging system lens built for the Cascade MicroTech probe station. A magnification of 5X was used to visualize all aforementioned WS₂ GBs. All as-obtained optical images were brightness/contrast enhanced to have better presentation of WS₂ GBs using an image processing tool, ImageJ. Raman and photoluminescence (PL) characterizations of treated WS₂ domains were conducted using a JY Horiba Labram Aramis imaging confocal Raman microscope at an excitation wavelength of 532 nm. SEM images taken for WS₂ GBs were generated from a Hitachi-4300 scanning electron microscope. Topological characterizations regarding WS₂ GBs were performed using Asylum Research MFP-3D Atomic Force Microscopy. The study of WS₂ GBs regarding TEM SAED patterns was carried using a JEOL 2100 high-resolution TEM operating at 80kV. The aberration-corrected TEM images were obtained from Oxford's JEOL JEM-2200MCO field-emission gun TEM, fitted with CEOS probe and image aberration correctors and a double Wien Filter monochromator operated at an accelerating voltage of 80kV. Electrical measurements were conducted on our home-made probe station equipped with two ultra-fine tungsten tips (Signatone, SE-T, 5 µm in diameter) and a Keithley source meter (2400-LV). Measurements were all done in room-temperature ambient conditions.

Supporting Information Available

A schematic of the CVD system set-up. Characteristic Raman and PL intensity profiles for monolayer WS₂ domains and films. Evolution of monolayer WS₂ domains with different timings or temperatures. Monolayer WS₂ domain damage due to further increase of heat treatment temperature or treating duration. Raman and PL 2D mappings for the isolated and conjunctive monolayer WS₂ domains that

were not thermally treated. Selected area electron diffraction (SAED) patterns across the WS₂ domains.

IV source-drain electrical measurements for untreated and treated WS₂ domains and GBs.

Acknowledgements

JHW thanks the support from the Royal Society.

References

1. Li, X.; Cai, W.; An, J.; Kim, S.; Nah, J.; Yang, D.; Piner, R.; Velamakanni, A.; Jung, I.; Tutuc, E.; *et al.* Large-Area Synthesis of High-Quality and Uniform Graphene Films on Copper Foils. *Science* **2009**, *324*, 1312-1314.
2. Li, X.; Magnuson, C. W.; Venugopal, A.; Tromp, R. M.; Hannon, J. B.; Vogel, E. M.; Colombo, L.; Ruoff, R. S. Large-Area Graphene Single Crystals Grown by Low-Pressure Chemical Vapor Deposition of Methane on Copper. *J. Am. Chem. Soc.* **2011**, *133*, 2816-2819.
3. Bae, S.; Kim, H.; Lee, Y.; Xu, X.; Park, J.; Zheng, Y.; Balakrishnan, J.; Lei, T.; Kim, H. R.; Song, Y. I.; *et al.* Roll-to-roll Production of 30-inch Graphene Films for Transparent Electrodes. *Nature Nanotechnology* **2010**, *5*, 574-578.
4. Zhou, H.; Yu, W. J.; Liu, L.; Cheng, R.; Chen, Y.; Huang, X.; Liu, Y.; Wang, Y.; Huang, Y.; Duan, X. Chemical Vapour Deposition Growth of Large Single Crystals of Monolayer and Bilayer Graphene. *Nature Communications* **2013**, *4*, 2096.
5. Wu, Y. A.; Fan, Y.; Speller, S.; Creeth, G. L.; Sadowski, J. T.; He, K.; Robertson, A. W.; Allen, C. S.; Warner, J. H. Large Single Crystals of Graphene on Melted Copper Using Chemical Vapor Deposition. *ACS Nano* **2012**, *6*, 5010-5017.
6. Wu, Y. A.; Robertson, A. W.; Schaeffel, F.; Speller, S. C.; Warner, J. H. Aligned Rectangular Few-Layer Graphene Domains on Copper Surfaces. *Chemistry of Materials* **2011**, *23*, 4543-4547.
7. Yu, Q.; Jauregui, L. A.; Wu, W.; Colby, R.; Tian, J.; Su, Z.; Cao, H.; Liu, Z.; Pandey, D.; Wei, D.; *et al.* Control and Characterization of Individual Grains and Grain Boundaries in Graphene Grown by Chemical Vapour Deposition. *Nature Materials* **2011**, *10*, 443-449.
8. van der Zande, A. M.; Huang, P. Y.; Chenet, D. A.; Berkelbach, T. C.; You, Y.; Lee, G.; Heinz, T. F.; Reichman, D. R.; Muller, D. A.; Hone, J. C. Grains and Grain Boundaries in Highly Crystalline Monolayer Molybdenum Disulphide. *Nature Materials* **2013**, *12*, 554-561.
9. Yazyev, O. V.; Louie, S. G. Electronic Transport in Polycrystalline Graphene. *Nature Materials* **2010**, *9*, 806-809.
10. Najmaei, S.; Amani, M.; Chin, M. L.; Liu, Z.; Birdwell, A. G.; O'Regan, T. P.; Ajayan, P. M.; Dubey, M.; Lou, J. Electrical Transport Properties of Polycrystalline Monolayer Molybdenum Disulfide. *ACS Nano* **2014**, *8*, 7930-7937.

11. Huang, P. Y.; Ruiz-Vargas, C. S.; van der Zande, A. M.; Whitney, W. S.; Levendoff, M. P.; Kevek, J. W.; Garg, S.; Alden, J. S.; Hustedt, C. J.; Zhu, Y.; *et al.* Grains and Grain Boundaries in Single-layer Graphene Atomic Patchwork Quilts. *Nature* **2011**, *469*, 389-392.
12. Kim, K.; Lee, Z.; Regan, W.; Kisielowski, C.; Crommie, M. F.; Zettl, A. Grain Boundary Mapping in Polycrystalline Graphene. *ACS Nano* **2011**, *5*, 2142-2146.
13. Rasool, H. I.; Song, E. B.; Allen, M. J.; Wassei, J. K.; Kaner, R. B.; Wang, K. L.; Weiller, B. H.; Gimzewski, J. K. Continuity of Graphene on Polycrystalline Copper. *Nano Letters* **2011**, *11*, 251-256.
14. Gao, L.; Guest, J. R.; Guisinger, N. P. Epitaxial Graphene on Cu(111). *Nano Letters* **2010**, *10*, 3512-3516.
15. Dinh Loc Duong; Han, G. H.; Lee, S. M.; Gunes, F.; Kim, E. S.; Kim, S. T.; Kim, H.; Quang Huy Ta; So, K. P.; Yoon, S. J.; *et al.* Probing Graphene Grain Boundaries with Optical Microscopy. *Nature* **2012**, *490*, 235-239.
16. Huang, J.; Pu, J.; Hsu, C.; Chiu, M.; Juang, Z.; Chang, Y.; Chang, W.; Iwasa, Y.; Takenobu, T.; Li, L. Large-Area Synthesis of Highly Crystalline WSe₂ Monolayers and Device Applications. *ACS Nano* **2014**, *8*, 923-930.
17. Rong, Y.; Fan, Y.; Koh, A. L.; Robertson, A. W.; He, K.; Wang, S.; Tan, H.; Sinclair, R.; Warner, J. H. Controlling Sulphur Precursor Addition for Large Single Crystal Domains of WS₂. *Nanoscale* **2014**, *6*, 12096-12103.
18. Wang, X.; Gong, Y.; Shi, G.; Chow, W. L.; Keyshar, K.; Ye, G.; Vajtai, R.; Lou, J.; Liu, Z.; Ringe, E.; *et al.* Chemical Vapor Deposition Growth of Crystalline Monolayer MoSe₂. *ACS Nano* **2014**, *8*, 5125-5131.
19. Zhang, J.; Yu, H.; Chen, W.; Tian, X.; Liu, D.; Cheng, M.; Xie, G.; Yang, W.; Yang, R.; Bai, X.; *et al.* Scalable Growth of High-Quality Polycrystalline MoS₂ Monolayers on SiO₂ with Tunable Grain Sizes. *ACS Nano* **2014**, *8*, 6024-6030.
20. Lee, Y.; Zhang, X.; Zhang, W.; Chang, M.; Lin, C.; Chang, K.; Yu, Y.; Wang, J. T.; Chang, C.; Li, L.; *et al.* Synthesis of Large-Area MoS₂ Atomic Layers with Chemical Vapor Deposition. *Adv Mater* **2012**, *24*, 2320-2325.
21. Chiu, M.; Li, M.; Zhang, W.; Hsu, W.; Chang, W.; Terrones, M.; Terrones, H.; Li, L. Spectroscopic Signatures for Interlayer Coupling in MoS₂-WSe₂ van der Waals Stacking. *ACS Nano* **2014**, *8*, 9649-9656.
22. Ramasubramaniam, A. Large Excitonic Effects in Monolayers of Molybdenum and Tungsten Dichalcogenides. *Physical Review B* **2012**, *86*, 115409.
23. Gutierrez, H. R.; Perea-Lopez, N.; Elias, A. L.; Berkdemir, A.; Wang, B.; Lv, R.; Lopez-Urias, F.; Crespi, V. H.; Terrones, H.; Terrones, M. Extraordinary Room-Temperature Photoluminescence in Triangular WS₂ Monolayers. *Nano Letters* **2013**, *13*, 3447-3454.

24. Tongay, S.; Fan, W.; Kang, J.; Park, J.; Koldemir, U.; Suh, J.; Narang, D. S.; Liu, K.; Ji, J.; Li, J.; *et al.* Tuning Interlayer Coupling in Large-Area Heterostructures with CVD-Grown MoS₂ and WS₂ Monolayers. *Nano Letters* **2014**, *14*, 3185-3190.
25. Zhang, W.; Chuu, C.; Huang, J.; Chen, C.; Tsai, M.; Chang, Y.; Liang, C.; Chen, Y.; Chueh, Y.; He, J.; *et al.* Ultrahigh-Gain Photodetectors Based on Atomically Thin Graphene-MoS₂ Heterostructures. *Scientific Reports* **2014**, *4*, 3826.
26. Zhang, W.; Chiu, M.; Chen, C.; Chen, W.; Li, L.; Wee, A. T. S. Role of Metal Contacts in High-Performance Phototransistors Based on WSe₂ Monolayers. *ACS Nano* **2014**, *8*, 8653-8661.
27. Chang, Y.; Zhang, W.; Zhu, Y.; Han, Y.; Pu, J.; Chang, J.; Hsu, W.; Huang, J.; Hsu, C.; Chiu, M.; *et al.* Monolayer MoSe₂ Grown by Chemical Vapor Deposition for Fast Photodetection. *ACS Nano* **2014**, *8*, 8582-8590.
28. Zhang, W.; Huang, J.; Chen, C.; Chang, Y.; Cheng, Y.; Li, L. High-Gain Phototransistors Based on a CVD MoS₂ Monolayer. *Adv Mater* **2013**, *25*, 3456-3461.
29. Zhang, Y.; Zhang, Y.; Ji, Q.; Ju, J.; Yuan, H.; Shi, J.; Gao, T.; Ma, D.; Liu, M.; Chen, Y.; *et al.* Controlled Growth of High-Quality Monolayer WS₂ Layers on Sapphire and Imaging Its Grain Boundary. *ACS Nano* **2013**, *7*, 8963-8971.
30. Ly, T. H.; Chiu, M.; Li, M.; Zhao, J.; Perello, D. J.; Cichocka, M. O.; Oh, H. M.; Chae, S. H.; Jeong, H. Y.; Yao, F.; *et al.* Observing Grain Boundaries in CVD-Grown Monolayer Transition Metal Dichalcogenides. *ACS Nano* **2014**, *8*, 11401-11408.
31. Ling, X.; Lee, Y.; Lin, Y.; Fang, W.; Yu, L.; Dresselhaus, M. S.; Kong, J. Role of the Seeding Promoter in MoS₂ Growth by Chemical Vapor Deposition. *Nano Letters* **2014**, *14*, 464-472.
32. Najmaei, S.; Liu, Z.; Zhou, W.; Zou, X.; Shi, G.; Lei, S.; Yakobson, B. I.; Idrobo, J.; Ajayan, P. M.; Lou, J. Vapour Phase Growth and Grain Boundary Structure of Molybdenum Disulphide Atomic Layers. *Nature Materials* **2013**, *12*, 754-759.
33. Nan, H.; Wang, Z.; Wang, W.; Liang, Z.; Lu, Y.; Chen, Q.; He, D.; Tan, P.; Miao, F.; Wang, X.; *et al.* Strong Photoluminescence Enhancement of MoS₂ through Defect Engineering and Oxygen Bonding. *ACS Nano* **2014**, *8*, 5738-5745.
34. Tongay, S.; Zhou, J.; Ataca, C.; Liu, J.; Kang, J. S.; Matthews, T. S.; You, L.; Li, J.; Grossman, J. C.; Wu, J. Broad-Range Modulation of Light Emission in Two-Dimensional Semiconductors by Molecular Physisorption Gating. *Nano Letters* **2013**, *13*, 2831-2836.
35. Peimyoo, N.; Shang, J.; Cong, C.; Shen, X.; Wu, X.; Yeow, E. K. L.; Yu, T. Nonblinking, Intense Two-Dimensional Light Emitter: Monolayer WS₂ Triangles. *ACS Nano* **2013**, *7*, 10985-10994.
36. Liu, Y.; Ghosh, R.; Wu, D.; Ismach, A.; Ruoff, R.; Lai, K. Mesoscale Imperfections in MoS₂ Atomic Layers Grown by a Vapor Transport Technique. *Nano Letters* **2014**, *14*, 4682-4686.
37. Zhou, W.; Zou, X.; Najmaei, S.; Liu, Z.; Shi, Y.; Kong, J.; Lou, J.; Ajayan, P. M.; Yakobson, B. I.; Idrobo, J. Intrinsic Structural Defects in Monolayer Molybdenum Disulfide. *Nano Letters* **2013**, *13*, 2615-2622.

TOC Graphic

